

Deep Generalization of Structured Low Rank Algorithms (Deep-SLR)

Aniket Pramanik, Hemant Aggarwal, Mathews Jacob
The University of Iowa, USA

Abstract—Structured low-rank (SLR) algorithms are emerging as powerful image reconstruction approaches because they can capitalize on several signal properties, which conventional image-based approaches have difficulty in exploiting. The main challenge with this scheme that self learns an annihilation convolutional filterbank from the undersampled data is its high computational complexity. We introduce a deep-learning approach to quite significantly reduce the computational complexity of SLR schemes. Specifically, we pre-learn a CNN-based annihilation filterbank from exemplar data, which is used as a prior in a model-based reconstruction scheme. The CNN parameters are learned in an end-to-end fashion by un-rolling the iterative algorithm. The main difference of the proposed scheme with current model-based deep learning strategies is the learning of non-linear annihilation relations in Fourier space using a model-based framework. The experimental comparisons show that the proposed scheme can offer similar performance as SLR schemes in the calibrationless parallel MRI setting, while reducing the run-time by around three orders of magnitude. We also combine the proposed scheme with image domain priors, which are complementary, thus further improving the performance over SLR schemes.

Index Terms—structured low rank, annihilation, deep learning

I. INTRODUCTION

The recovery of images from highly undersampled multi-channel Fourier measurements is a classical problem in MRI [1]. The popular approach is to regularize the image recovery using priors that capture the image properties. Structured low-rank matrix completion approaches [2], [3] have been recently introduced to exploit properties of continuous domain signals, which are often difficult to be accounted by classical compressive sensing and low-rank methods. These methods rely on a lifting of the Fourier coefficients of the signal to a higher dimensional structured matrix; the structure of the lifted matrix is designed to exploit specific signal properties. These methods exploit the dual relationship between signal property and rank of the lifted matrix. SLR methods have been shown to be very efficient in capitalizing on support constraints [3], continuous domain sparsity [4], [5], phase [3], multi-channel relations in parallel MRI [6] as well as multi-shot acquisitions [7], and exponential structure of MRI time series [2]. Recent iterative reweighted least-square (IRLS) SLR algorithms make use of the convolutional structure of the structured matrices [8] to accelerate the algorithms. These methods

alternates between the the estimation of an annihilation (null-space) filterbank, followed by updating the Fourier coefficients of the signal from the available measurements using the annihilation filterbank. Specifically, the Fourier coefficients are chosen such that they matches the measurements, while the energy of the projection to the null-space is minimized; the projection to signal-subspace is achieved using a residual convolution-deconvolution filter bank, which serves as a denoiser. While this algorithm is considerably faster than earlier approaches, the iterative estimation of the annihilation filterbank from the undersampled data is still computationally expensive. An approach to reduce the computational complexity is to estimate the null-space filters from a fully-sampled calibration region [4], [3]. Since the annihilation filterbank need not be derived from the undersampled data in an iterative fashion, this approach offers faster reconstructions. However, the challenge with these methods is the need for a calibration region, which restricts the achievable acceleration.

Several researchers have introduced image domain deep learning as a fast and efficient alternative to compressed sensing reconstructions. Direct inversion approaches, which learns to reconstruct a sub-class of images from the measured data [9], [10], [11], and model based algorithms that use a forward model of the imaging physics combined with a deep-learned prior [12], [13], [14] have been proposed. A challenge with direct inversion schemes is the large network that is needed to invert the image acquisition scheme, which translate to large number of trainable parameters and large training data demand [9], [15]. The use of the forward model within model based schemes allows the use much smaller networks to model the image priors, which significantly reduces the run time. The improvement in image quality with multiple iterations of optimization blocks, sharing weights across network, and end-to-end training have been demonstrated, and the ability to use multiple learned regularization priors [14].

In this paper, we introduce a general deep learning strategy to reduce the run-time of the SLR algorithms. We propose to replace the residual convolution-deconvolution linear filter bank in the IRLS SLR algorithm by a residual multichannel convolution neural network (CNN). The improved representation power of CNN allows us to learn a generalizable projection operator from exemplar data. Specifically, during inference the residual CNN behaves as a projection for each dataset, facilitating the *denoising* of the dataset from alias artifacts and noise. The framework is motivated by the IRLS implementation of SLR algorithms, and its similarity to the MoDL framework. Similar to MoDL, we unroll the resulting

Aniket Pramanik, Hemant Aggarwal and Mathews Jacob are from the Department of Electrical and Computer Engineering at the University of Iowa, Iowa City, IA, 52242, USA (e-mail: aniket-pramanik@uiowa.edu; hemantkumar-aggarwal@uiowa.edu; mathews-jacob@uiowa.edu). This work is supported by grant NIH 1R01EB019961-01A1.

algorithm and learn the parameters of the non-linear filter bank in an end-to-end fashion. Since the parameters of the filterbank need not be estimated from the data itself, very few iterations are needed for convergence during image recovery. We also propose to combine this approach with an image domain prior similar to MoDL, which is complementary to the Fourier domain multichannel relations. This hybrid approach offers improved performance over SLR, while offering around three orders of magnitude reduction in computational complexity.

We focus on two representative applications—sparse single channel recovery and parallel MRI—that use two distinct lifting structures used in the SLR setting [2]. Specifically, we show how different liftings can be accommodated in the proposed scheme by modifying the data organization of the input and output of the CNN module. This enables the extension of the proposed framework to a range of SLR applications [2], [3], [16], which use one of the above lifting structures or their combinations.

This work is related to our previous work on correcting phase errors in multi-shot diffusion weighted acquisition [17]. The main focus of this work is to generalize the above approach for general SLR liftings and demonstrate its utility in applications beyond the diffusion setup. This work extends the preliminary work in [18]. In particular, we consider parallel MRI and the exploitation of continuous domain sparsity in this paper, which are not considered in [17]. We note that the use of deep learning methods in k-space were recently studied in [19], [15], [11]. The RAKI framework [11] is a calibrated scheme unlike our calibration-free approach. A direct inversion (model-free) approach was pursued in [19], which is different from the proposed model-based framework which also combines image domain priors. The KIKI net approach [15] was only introduced for single channel setting unlike our uncalibrated multi-channel scheme. The proposed reconstructions are compared against model-free image domain deep-learning [9], k-space deep-learning [19], image domain MoDL [14] and traditional SLR methods. These comparisons reveal the improved performance offered by the Deep-SLR framework.

II. BACKGROUND

We now briefly describe the background to make the paper self-contained and easily accessible.

A. Forward model

We model the acquisition of image $\rho[\mathbf{r}]$ as:

$$\mathbf{b}_i = \mathcal{A} \left(\mathcal{F} \left(\underbrace{s_i \rho}_{\rho_i} \right) \right) + \boldsymbol{\eta}_i, \quad i = 1 \dots N, \quad (1)$$

where s_i ; $i = 1, \dots, N$ is the coil sensitivity of the i^{th} coil, while \mathbf{b}_i and $\boldsymbol{\eta}_i$ are multi-channel noisy under-sampled Fourier measurements and zero mean additive white Gaussian noise. Here \mathcal{F} is the Fourier transform that maps ρ_i onto the k-space samples and \mathcal{A} is a linear undersampling operator. We compactly denote the above operation as

$$\mathbf{B} = \mathcal{A}(\hat{\rho}) + \boldsymbol{\eta} \quad (2)$$

where $\hat{\rho} = [\hat{\rho}_1 \dots \hat{\rho}_N]$ is the multi-channel Fourier data.

B. Structured Low-Rank algorithms

SLR methods rely on different liftings of the Fourier coefficients, designed to exploit specific properties of the signal. We now discuss two representative SLR applications, which consider the different type of liftings used in the SLR setting.

1) *Continuous domain sparsity*: A continuous domain piecewise constant image ρ with edges specified by the zero sets of a bandlimited function η satisfies an image domain annihilation relation, $\nabla \rho(\mathbf{r}) \cdot \eta(\mathbf{r}) = 0, \forall \mathbf{r}$ where \mathbf{r} represents spatial co-ordinates. Here, $\nabla(\cdot)$ denotes the gradient of f . This relation translates to the following Fourier domain annihilation relations $\widehat{\nabla \rho}[\mathbf{k}] * n[\mathbf{k}] = 0, \forall \mathbf{k}$ where \mathbf{k} denotes k-space (Fourier space). Here $\widehat{\nabla \rho}[\mathbf{k}]$ are the Fourier coefficients of the gradient of ρ and $n[\mathbf{k}]$ is the Fourier transform of $\eta(\mathbf{r})$. We denote the mapping from the Fourier coefficients $\hat{\rho}$ to $\widehat{\nabla \rho}$ by \mathcal{G} :

$$\mathcal{G}(\hat{\rho}) = \widehat{\nabla \rho}[\mathbf{k}] = \begin{bmatrix} j2\pi k_x \hat{\rho}[\mathbf{k}] \\ j2\pi k_y \hat{\rho}[\mathbf{k}] \end{bmatrix} = \begin{bmatrix} \hat{\rho}_x \\ \hat{\rho}_y \end{bmatrix}. \quad (3)$$

Note that \mathcal{G} essentially creates two copies of $\hat{\rho}$, each with a different Fourier weighting.

The convolution relation $\widehat{\nabla \rho}[\mathbf{k}] * n[\mathbf{k}] = 0$ can be represented as Hankel matrix multiplication $\mathcal{H}(\widehat{\nabla \rho}) \mathbf{n} = 0$. The number of such null-space filters M is often large (see [20])

$$\underbrace{\begin{bmatrix} \mathcal{H}(\hat{\rho}_x) \\ \mathcal{H}(\hat{\rho}_y) \end{bmatrix}}_{\mathcal{T}(\mathcal{G}(\hat{\rho}))} \underbrace{[\mathbf{n}_1 \mid \mathbf{n}_2 \mid \dots \mid \mathbf{n}_M]}_{\mathbf{N}} = 0. \quad (4)$$

resulting in a low-rank matrix $\mathcal{T}(\mathcal{G}(\hat{\rho}))$.

Note that the Hankel matrices are vertically stacked to obtain $\mathcal{T}(\mathcal{G}(\hat{\rho}))$, which is a common approach in SLR [6].

2) *Parallel MRI acquisition scheme*: Image and Fourier domain multi-channel annihilation relations were shown in [6], [2]. Specifically each pair of multichannel images in (1) satisfy a Fourier domain annihilation relation $\hat{\rho}_i[\mathbf{k}] * \hat{s}_j[\mathbf{k}] - \hat{\rho}_j[\mathbf{k}] * \hat{s}_i[\mathbf{k}] = 0, \forall \mathbf{k}$, where $\hat{\rho}_i[\mathbf{k}]$ and $\hat{s}_i[\mathbf{k}]$ are the Fourier coefficients of $\rho_i(\mathbf{k})$ and $s_i(\mathbf{k})$ respectively. Such annihilation relations exist for every pair of coil images, and can be compactly written as,

$$\underbrace{[\mathcal{H}(\hat{\rho}_1) \quad \mathcal{H}(\hat{\rho}_2) \quad \dots \quad \mathcal{H}(\hat{\rho}_N)]}_{\mathcal{T}(\hat{\rho})} \cdot \mathbf{N} = 0. \quad (5)$$

The columns of N correspond to the vertical stacking of the filters \hat{s}_i . The large null space \mathbf{N} implies it is low rank. Note that the Hankel matrices are horizontally stacked to obtain $\mathcal{T}(\hat{\rho})$. Here $\mathcal{G} = \mathcal{I}$, which is the identity mapping. This is another popular class of liftings used in SLR [6], [2], [3].

C. Calibration-free SLR methods

In the general setting, SLR schemes aim to recover an image or a series of images ρ from its measurements $\mathcal{A}(\hat{\rho})$ by solving the optimization problem:

$$\min_{\hat{\rho}} \text{rank} [\mathcal{T}(\mathcal{G}(\hat{\rho}))] \text{ such that } \mathbf{b} = \mathbf{A}\hat{\rho} + \boldsymbol{\eta}. \quad (6)$$

Here, $\mathcal{T}(\cdot)$ is a lifting operator than lifts the weighted signal $\mathcal{G}(\hat{\rho})$ into a higher dimensional structured matrix. As discussed

before, the generic weighting matrix \mathcal{G} depends on the specific annihilation relation. The recovery of $\hat{\rho}$ is often posed as an unconstrained nuclear norm minimization problem

$$\arg \min_{\hat{\rho}} \|\mathcal{A}(\hat{\rho}) - \mathbf{b}\|_2^2 + \lambda \|\mathcal{T}(\mathcal{G}(\hat{\rho}))\|_* \quad (7)$$

where λ is a regularizer to tune the nuclear norm loss term.

D. Iterative reweighted least-squares (IRLS) algorithm

The IRLS scheme majorizes nuclear norm with weighted Frobenius norm as $\|\mathcal{T}(\mathcal{G}(\hat{\rho}))\|_* \leq \|\mathcal{T}(\mathcal{G}(\hat{\rho}))\mathbf{Q}\|_F^2$ to yield a two-variable optimization problem

$$\arg \min_{\hat{\rho}, \mathbf{Q}} \|\mathcal{A}(\hat{\rho}) - \mathbf{b}\|_2^2 + \lambda \|\mathcal{T}(\mathcal{G}(\hat{\rho}))\mathbf{Q}\|_F^2, \quad (8)$$

which alternates between the null-space \mathbf{Q} and image $\hat{\rho}$,

$$\hat{\rho}^{(n)} = \arg \min_{\hat{\rho}} \|\mathcal{A}(\hat{\rho}) - \mathbf{b}\|_2^2 + \lambda \|\mathcal{T}(\mathcal{G}(\hat{\rho}))\mathbf{Q}^{(n-1)}\|_F^2 \quad (9)$$

$$\mathbf{Q}^{(n)} = [\mathcal{T}(\mathcal{G}(\hat{\rho}^{(n)}))^H \mathcal{T}(\mathcal{G}(\hat{\rho}^{(n)})) + \epsilon^{(n)} \mathbf{I}]^{\frac{n}{2}-1} \quad (10)$$

respectively. The matrix \mathbf{Q} can be viewed as a collection of column vectors spanning the null space of $\mathcal{T}(\mathcal{G}(\hat{\rho}))$.

E. Calibration based SLR methods

Several calibration based MRI schemes (e.g. GRAPPA, SPIRIT [21], [22], [4]) can be viewed as a special case of the SLR schemes. These approaches acquire a fully-sampled calibration region in the Fourier domain, which correspond to fully-sampled rows of $\mathcal{T}(\mathcal{G}(\hat{\rho}))$, or equivalently the sub-matrix $\mathcal{T}_R(\mathcal{G}(\hat{\rho}))$. These schemes estimate the null-space matrix \mathbf{Q} by minimizing $\|\mathcal{T}_R(\mathcal{G}(\hat{\rho}))\mathbf{Q}\|_F^2$ subject to norm constraints on \mathbf{Q} .

Once the \mathbf{Q} is pre-estimated from calibration data, the image is recovered from undersampled Fourier coefficients as

$$\hat{\rho} = \arg \min_{\hat{\rho}} \|\mathcal{A}(\hat{\rho}) - \mathbf{b}\|_2^2 + \lambda \|\mathcal{T}(\mathcal{G}(\hat{\rho}))\mathbf{Q}\|_F^2 \quad (11)$$

The above optimization problem can be solved analytically for specific sampling patterns [21], [6]. In other cases such as [22], [4], [3], the above problem is solved iteratively. Both strategies are computationally efficient since \mathbf{Q} is fully known. However, the need for calibration restricts the achievable acceleration.

III. DEEP GENERALIZATION OF SLR METHODS

The main focus of this work is to introduce a deep-learning solution to improve the computational efficiency of SLR algorithms. We note that calibrated SLR methods, which learn the linear null-space projection operator from calibration data, require few iterations for convergence, thus offer fast image recovery. Calibration-free SLR methods by contrast are computationally expensive. Specifically, because the null-space matrix \mathbf{Q} is estimated from the data itself, the algorithm requires several iterations to converge.

We propose to pre-learn a CNN based null-space projector from multiple exemplar datasets. We hypothesize that the deep-learning based operator can act as a linear projector to the null-space for each of the datasets; the use of the associated prior term as a regularizer would result in an algorithm with the computational efficiency of calibrated methods, while not requiring the acquisition of a fully-sampled calibrated region.

A. IRLS algorithm with variable splitting

To facilitate the reinterpretation of the reconstruction scheme as an iterative denoising strategy, we introduce an auxiliary variable $\hat{\mathbf{z}}$ in (8) to obtain a three-variable constrained optimization problem,

$$\arg \min_{\hat{\rho}, \mathbf{Q}, \hat{\mathbf{z}}} \|\mathcal{A}(\hat{\rho}) - \mathbf{b}\|_2^2 + \lambda \|\mathcal{T}(\hat{\mathbf{z}})\mathbf{Q}\|_F^2 \text{ such that } \hat{\mathbf{z}} = \mathcal{G}(\hat{\rho}). \quad (12)$$

We impose the constraint by a penalty term as

$$\arg \min_{\hat{\rho}, \mathbf{Q}, \hat{\mathbf{z}}} \|\mathcal{A}(\hat{\rho}) - \mathbf{b}\|_2^2 + \lambda \|\mathcal{T}(\hat{\mathbf{z}})\mathbf{Q}\|_F^2 + \beta \|\mathcal{G}(\hat{\rho}) - \hat{\mathbf{z}}\|_2^2.$$

This formulation is equivalent to (12) when $\beta \rightarrow \infty$. We propose to solve the above problem using the alternating minimization scheme:

$$\hat{\rho}_{n+1} = \arg \min_{\hat{\rho}} \|\mathcal{A}(\hat{\rho}) - \mathbf{b}\|_2^2 + \beta \|\mathcal{G}(\hat{\rho}) - \hat{\mathbf{z}}_n\|_2^2 \quad (13)$$

$$\hat{\mathbf{z}}_{n+1} = \arg \min_{\hat{\mathbf{z}}} \beta \|\mathcal{G}(\hat{\rho}_{n+1}) - \hat{\mathbf{z}}\|_2^2 + \lambda \|\mathcal{T}(\hat{\mathbf{z}})\mathbf{Q}\|_F^2. \quad (14)$$

At each step, the \mathbf{Q} matrix is updated as in (10).

1) *Image sub-problem*: The first step specified by (13) is a simple Tikhonov regularized optimization problem to recover the images ρ at the $(n+1)$ -th iteration. When $\mathcal{G} = \mathcal{I}$, the prior reduces to $\|\hat{\rho} - \hat{\mathbf{z}}_n\|_2^2$. In the general case, the solution to this optimization problem can be determined analytically as

$$\hat{\rho}_n = (\mathcal{A}^H \mathcal{A} + \beta \mathcal{G}^H \mathcal{G})^{-1} (\mathcal{A}^H \mathbf{b} + \beta \mathcal{G}^H (\hat{\mathbf{z}}_{n-1})), \quad (15)$$

when \mathcal{A} involves a sampling in the Fourier domain. Similar analytical solutions can also be used when \mathcal{G} involves a Fourier domain weighting as in [23].

2) *Denoising sub-problem*: The sub-problem (14) is essentially a proximal operation. Specifically, the second term of (14) is the energy in projecting $\mathcal{T}(\hat{\mathbf{z}})$ to the subspace \mathbf{Q} . If $\lambda \rightarrow \infty$, we obtain $\hat{\mathbf{z}}$ as the projection of $\hat{\rho}_{n+1}$ onto the signal subspace, orthogonal to \mathbf{Q} .

B. Filterbank interpretation of the denoising subproblem

We will now focus on the denoising sub-problem by showing its linear filterbank structure. We will capitalize on this structure to generalize the algorithm. We will focus on the vertical and horizontal stacking cases separately.

1) *Vertical stacking*: Consider the term $\mathcal{T}(\hat{\mathbf{z}})\mathbf{q}_i$, where \mathbf{q}_i is one of the columns of the matrix \mathbf{Q} . When the lifting operation is described by (4), we have

$$\mathcal{T}(\hat{\mathbf{z}})\mathbf{q}_i = \begin{bmatrix} \mathcal{H}(\hat{\mathbf{z}}_1) \\ \mathcal{H}(\hat{\mathbf{z}}_2) \end{bmatrix} \mathbf{q}_i = \begin{bmatrix} \mathbf{p}_1 \\ \mathbf{p}_2 \end{bmatrix} \quad (16)$$

Because $\mathcal{H}(\hat{\mathbf{z}})$ is a Hankel matrix, $\mathcal{H}(\hat{\mathbf{z}})\mathbf{q}$ corresponds to the linear convolution between $\hat{\mathbf{z}}$ and \mathbf{q} . Since convolution is commutative, we can rewrite the above expression as

$$\mathcal{T}(\hat{\mathbf{z}})\mathbf{q}_i = \underbrace{\begin{bmatrix} \hat{\mathbf{z}}_1 \\ \hat{\mathbf{z}}_2 \end{bmatrix}}_{\hat{\mathbf{z}}} \mathcal{P}(\mathbf{q}_i), \quad (17)$$

where, $\mathcal{P}(\mathbf{q}_i)$ is a block Hankel matrix constructed from the samples of \mathbf{q}_i . We thus have $\|\mathcal{T}(\hat{\mathbf{z}})\mathbf{Q}\|_F^2 = \|\hat{\mathbf{z}} \mathcal{S}(\mathbf{Q})\|_F^2$, where

$S(\mathbf{Q})$ is obtained by horizontally stacking the matrices $\mathcal{P}(\mathbf{q}_i)$. We note that $\hat{\mathbf{z}}_1 S(\mathbf{Q})$ corresponds to passing $\hat{\mathbf{z}}_1$ through a single input multiple output (SIMO) filter bank, whose filters are specified by \mathbf{q}_i .

2) *Horizontal stacking*: Similar to the vertical stacking case, we consider

$$\begin{aligned} \mathcal{T}(\hat{\mathbf{z}}) \mathbf{q}_i &= \overbrace{\begin{bmatrix} \mathcal{H}(\hat{\mathbf{z}}_1) & \dots & \mathcal{H}(\hat{\mathbf{z}}_N) \end{bmatrix}}^{\mathcal{T}(\hat{\mathbf{z}})} \overbrace{\begin{bmatrix} \mathbf{q}_{i,1} \\ \vdots \\ \mathbf{q}_{i,N} \end{bmatrix}}^{\mathbf{q}_i} \\ &= \begin{bmatrix} \mathcal{P}(\mathbf{q}_{i,1}) & \dots & \mathcal{P}(\mathbf{q}_{i,N}) \\ \vdots & \dots & \vdots \\ \mathcal{P}(\mathbf{q}_{N,1}) & \dots & \mathcal{P}(\mathbf{q}_{N,N}) \end{bmatrix} \begin{bmatrix} \hat{\mathbf{z}}_1 \\ \vdots \\ \hat{\mathbf{z}}_N \end{bmatrix} \end{aligned} \quad (18)$$

$$= \begin{bmatrix} \mathcal{P}(\mathbf{q}_{1,1}) & \dots & \mathcal{P}(\mathbf{q}_{1,N}) \\ \vdots & \dots & \vdots \\ \mathcal{P}(\mathbf{q}_{N,1}) & \dots & \mathcal{P}(\mathbf{q}_{N,N}) \end{bmatrix} \begin{bmatrix} \hat{\mathbf{z}}_1 \\ \vdots \\ \hat{\mathbf{z}}_N \end{bmatrix} \quad (19)$$

We thus have $\|\mathcal{T}(\hat{\mathbf{z}})\mathbf{Q}\|^2 = \|S(\mathbf{Q})\hat{\mathbf{z}}\|^2$, where

$$S(\mathbf{Q}) = \begin{bmatrix} \mathcal{P}(\mathbf{q}_{1,1}) & \dots & \mathcal{P}(\mathbf{q}_{1,N}) \\ \vdots & \dots & \vdots \\ \mathcal{P}(\mathbf{q}_{N,1}) & \dots & \mathcal{P}(\mathbf{q}_{N,N}) \end{bmatrix} \quad (20)$$

We note that $S(\mathbf{Q})\hat{\mathbf{z}}$ corresponds to passing $\hat{\mathbf{z}}$ through a multiple input multiple output (MIMO) filter bank, whose filters are specified by \mathbf{q}_i .

C. Approximation of denoising sub-problem

We thus rewrite (14) for both lifting approaches as,

$$\hat{\mathbf{z}}_{n+1} = \arg \min_{\hat{\mathbf{z}}} \beta \|\mathcal{G}(\hat{\rho}_{n+1}) - \hat{\mathbf{z}}\|^2 + \lambda \|S(\mathbf{Q})\hat{\mathbf{z}}\|_F^2. \quad (21)$$

which reduces to

$$\hat{\mathbf{z}}_{n+1} = \left[\mathbf{I} + \frac{\lambda}{\beta} S(\mathbf{Q}_n)^H S(\mathbf{Q}_n) \right]^{-1} \mathcal{G}(\hat{\rho}_{n+1}). \quad (22)$$

We propose to solve the denoising problem approximately. Assuming $\lambda \ll \beta$ and applying matrix inversion lemma, we obtain an approximate solution for $\hat{\mathbf{z}}$ as,

$$\hat{\mathbf{z}}_{n+1} \approx \underbrace{\left[\mathbf{I} - \frac{\lambda}{\beta} \overbrace{S(\mathbf{Q}_n)^H S(\mathbf{Q}_n)}^{R_n} \right]}_{\mathcal{L}_n} \mathcal{G}(\hat{\rho}_{n+1}) \quad (23)$$

As discussed before, $S(\mathbf{Q})$ denotes a MIMO or SIMO filterbank, depending on the nature of lifting. The term $S(\mathbf{Q})^H$ denotes convolution with flipped version of \mathbf{Q} , often referred to as deconvolution layer in deep learning literature. \mathcal{R}_n is a filter bank that projects the signal to the null-space, thus killing or annihilating the signal and preserving the noise terms. Thus, the linear operator \mathcal{L}_n is a residual block, which removes the alias or noise terms from the input signal, thus essentially denoising the signal (see Fig. 1).

Note that the filterbank \mathbf{Q}_n has a subscript n since it is updated at every iteration. The joint estimation of \mathbf{Q}_n and reconstruction $\hat{\rho}_n$ results in high computational complexity. On the other hand, calibration-based methods pre-estimate \mathbf{Q} and hence the residual filterbank \mathcal{L} , thus resulting in significantly reduced computational complexity.

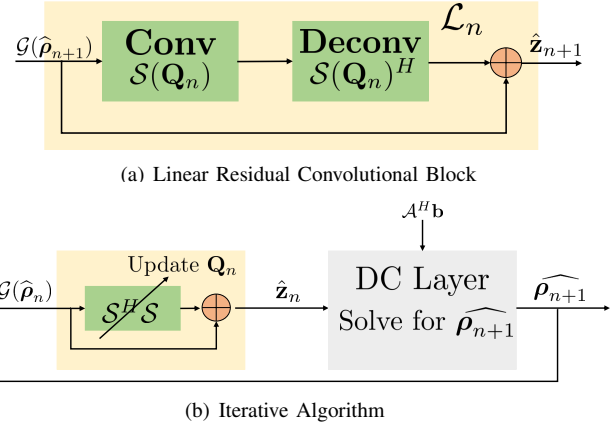


Fig. 1. Illustration of the network structure of the IRLS algorithm used in structured low-rank algorithms. (a) shows the linear residual convolutional-deconvolutional block, which projects the signal at the n^{th} iteration to the signal subspace. (b) illustrates the network-structure of the SLR algorithm, which alternates between the projection and the data consistency block. We note that in calibration-based approaches, the filter parameters of the projection block \mathcal{L} are fixed and are estimated from the calibration data. By contrast, the filter parameters are updated at each iteration based on the current iterate $\hat{\rho}_n$.

D. SLR-inspired model based k-space deep learning

The main disadvantage with the IRLS strategy discussed above is the high computational complexity. Specifically, this iterative approach requires an SVD at each iteration, and thus results in a computationally expensive algorithm. To improve the computational efficiency, we propose to pre-learn a non-linear convolutional neural network (CNN) annihilation filterbank \mathcal{N}_k from exemplar data. The subscript k indicates that the network performs convolutions in k -space. We pose the reconstruction similar to (11) as

$$\arg \min_{\hat{\rho}} \|\mathcal{A}(\hat{\rho}) - \mathbf{b}\|_2^2 + \lambda \left\| \underbrace{(\mathcal{I} - \mathcal{D}_k)}_{\mathcal{N}_k} (\mathcal{G}(\hat{\rho})) \right\|_2^2. \quad (24)$$

Here, \mathcal{N}_k is a CNN which kills or annihilates the signal, while it preserves the noise or alias terms, which is conceptually similar to \mathcal{R}_n in (23). Thus, the operator $\mathcal{D}_k = \mathcal{I} - \mathcal{N}_k$ can be viewed as a denoiser similar to \mathcal{L}_n in (23).

We propose to pre-learn the parameters of the network from exemplar data. Unlike calibrated schemes that learn a small linear network from a small subset of Fourier data (calibration region), the CNN parameters are learned from several fully-sampled exemplar datasets. This approach enables us to learn a larger CNN, which can generalize to other datasets. We hypothesize that this pre-learned non-linear network can behave like a linear projection for each dataset, thereby facilitating their recovery from undersampled data. Since the parameters of the network do not need to be self-learned, this approach is significantly faster than uncalibrated SLR approaches.

We use an alternating minimization strategy similar to (13) and (14) to minimize (24). The resulting algorithm translates to a recursive network, which alternates between the denoising network \mathcal{D}_k , which removes the noise and alias terms, and data

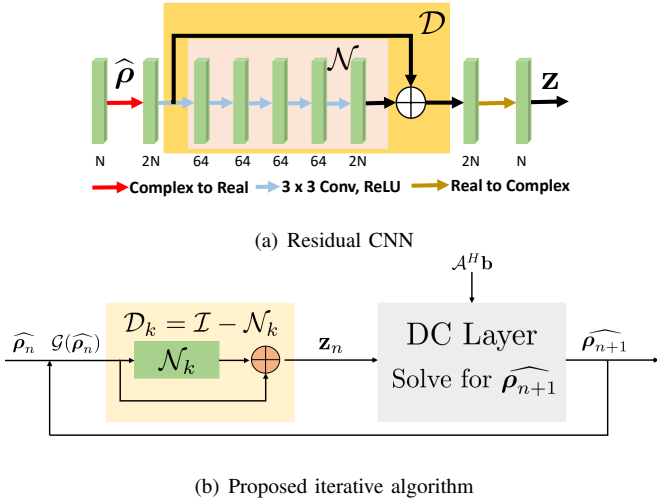


Fig. 2. Network structure of the proposed recursive CNN in k-space, described in Section III-D. The main difference of the proposed scheme with the approach in Fig. 1 is the use of the deep residual CNN in (b), instead of the linear convolution-deconvolution block in Fig. 1.(a). For implementation purposes, we split the real and imaginary part of the input k-space data into real and imaginary components, which are fed as two channels. The two output channels are combined together to recreate the complex output k-space data. We set $N = 1$ in the single image setting considered in Section II-B1, while N is the number of channels in the parallel MRI setting. Another key difference with the approach in Fig. 1 is that the CNN parameters are fixed and do not change with iterations as in Fig. 1.(b). The pre-learning of the CNN parameters using exemplar data allows us to significantly reduce the number of alternating steps compared to the self-learning strategy in Fig. 1. consistency (DC) blocks:

$$\hat{\mathbf{z}}_n = \mathcal{D}_k(\mathcal{G}\hat{\rho}_n) \quad (25)$$

$$\hat{\rho}_{n+1} = (\mathcal{A}^H \mathcal{A} + \lambda \mathcal{G}^H \mathcal{G})^{-1} (\mathcal{A}^H \mathbf{b} + \lambda \mathcal{G}^H \hat{\mathbf{z}}_n) \quad (26)$$

Similar to [14], we consider K iterations of the above algorithm and unroll the above iterative scheme to obtain a deep network. The unrolled network consists of K number of repetitions of both \mathcal{D}_k and DC blocks with parameters of \mathcal{D}_k being shared across iterations. At each iteration, the *noisy* input $\mathcal{G}\hat{\rho}_n$ is projected to the signal subspace and hence denoised. The output of \mathcal{D}_k is given by $\mathcal{D}_k(\mathcal{G}\hat{\rho}_n) = \mathcal{G}\hat{\rho}_n - \mathcal{N}_k(\mathcal{G}\hat{\rho}_n)$. The output is then fed into the data-consistency block as shown in Fig 2. As discussed previously, this iterative algorithm is similar to an alternating scheme to solve (11), with the distinction that the linear convolution-deconvolution block is replaced by a non-linear CNN. Unlike the setting in (11), where the filter parameters are learned from calibration data of each dataset, we propose to pre-learn a CNN from exemplary data.

E. Hybrid Regularized Deep learning

The structured low-rank methods exploit the redundancies in k-space resulting from specific structures in the signal. However, we note that the image patches in MR images often has extensive redundancy, which is exploited in our MoDL scheme [14] as well as other image domain methods [24], [25]. These priors are complementary to the SLR priors we discussed in the previous section. We propose to modify the cost function in (24) as,

$$\arg \min_{\hat{\rho}} \|\mathcal{A}\hat{\rho} - \mathbf{b}\|_2^2 + \lambda \|\mathcal{N}_k(\mathcal{G}(\hat{\rho}))\|_2^2 + \beta \|\mathcal{N}_I(\hat{\rho})\|_2^2. \quad (27)$$

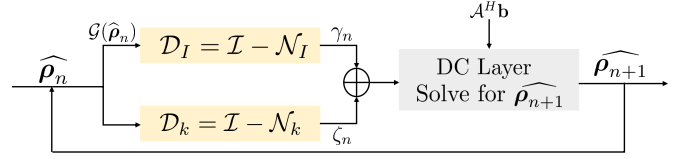


Fig. 3. Hybrid network: It consists of two identically structured residual CNNs $\mathcal{D}_k, \mathcal{D}_I$ for k-space and image domain learning respectively. The \mathcal{D}_I block learns redundancies in patches while \mathcal{D}_k block exploits k-space annihilation relations. The \mathcal{D}_I block does an IFFT on input k-space $\hat{\rho}$ and passes it to the residual CNN. The residual image output is transformed back to k-space $\hat{\rho}$ by an FFT. The output of \mathcal{D}_k and \mathcal{D}_I at n^{th} iteration are denoted by ζ_n and γ_n according to (28), (29) and (30). The parameters are not shared between \mathcal{D}_k and \mathcal{D}_I . Both \mathcal{D}_k and \mathcal{D}_I in hybrid Deep-SLR has half the number of feature maps per layer compared to \mathcal{D}_k in k-space Deep-SLR to keep the number of trainable parameters same in both the networks for fair comparisons. The network parameters are shared across iterations similar to the MoDL [14] framework.

Here, \mathcal{N}_I and \mathcal{N}_k are two residual CNNs. The alternating minimization of this scheme results in the following steps:

$$\zeta_n = \mathcal{D}_k(\mathcal{G}\hat{\rho}_n) \quad (28)$$

$$\gamma_n = \mathcal{D}_I(\hat{\rho}_n) \quad (29)$$

$$\hat{\rho}_{n+1} = (\mathcal{A}^H \mathcal{A} + \lambda \mathcal{G}^H \mathcal{G} + \beta \mathcal{I})^{-1} (\mathcal{A}^H \mathbf{b} + \lambda \mathcal{G}^H \zeta_n + \beta \gamma_n) \quad (30)$$

as shown in Fig 3. The \mathcal{D}_k relies on annihilation relations in k-space while \mathcal{D}_I exploits the image domain priors.

F. Special cases

We show application of our proposed methods in both single-channel and multi-channel setting, and show that the image sub-problem can be solved analytically in both cases. This approach will accelerate the training and testing procedures.

1) *Piecewise constant image structure*: The GIRAF algorithm is an SLR scheme which exploits the piecewise constant nature of images, described in Section II-B1. Here, the operator $\mathcal{G}(\hat{\rho}) = \widehat{\nabla} \hat{\rho}$ as defined in (3). In this case, we have

$$\mathcal{G}^H \begin{bmatrix} \hat{\mathbf{z}}_1 \\ \hat{\mathbf{z}}_2 \end{bmatrix} [\mathbf{k}] = -(j2\pi k_x \hat{\mathbf{z}}_1[\mathbf{k}] + j2\pi k_y \hat{\mathbf{z}}_2[\mathbf{k}]) \quad (31)$$

$$\mathcal{G}^H \mathcal{G}(\hat{\rho}) [\mathbf{k}] = 4\pi^2 (k_x^2 + k_y^2) \hat{\rho}[\mathbf{k}] \quad (32)$$

Note that the matrix $(\mathcal{A}^H \mathcal{A} + \lambda \mathcal{G}^H \mathcal{G} + \beta \mathcal{I})$ in (30) can be viewed as a weighting operator in the Fourier domain in the single-channel setting. We can thus solve (30) analytically.

2) *Parallel MRI acquisition*: In parallel MRI setting, $\mathcal{G} = \mathcal{I}$ and hence the data consistency term simplifies to $(\mathcal{A}^H \mathcal{A} + (\lambda + \beta) \mathcal{I})^{-1} (\mathcal{A}^H \mathbf{b} + \lambda \zeta_n + \beta \gamma_n)$. We note that $(\mathcal{A}^H \mathcal{A} + (\lambda + \beta) \mathcal{I})$ is separable across the channels. Hence, one can independently solve for each channel of $\hat{\rho}_{n+1}$ in the Fourier domain in an analytical fashion.

IV. EXPERIMENTAL DETAILS

A. Data Acquisition

We used the publicly available single-channel brain data from Human Connectome Project (HCP) and knee data from

Organ	Knee Sagittal		Knee Coronal		Brain (HCP)	
Acceleration	4x		6x		4x	
Methods	SNR	SSIM	SNR	SSIM	SNR	SSIM
GIRAF	18.14	0.841	19.01	0.877	20.02	0.912
K-UNET	17.76	0.830	18.78	0.872	17.78	0.838
K-space	18.69	0.849	19.16	0.878	19.18	0.897
I-UNET	17.29	0.834	18.53	0.873	17.43	0.832
Hybrid	19.31	0.852	22.48	0.921	23.39	0.925

TABLE I
QUANTITATIVE COMPARISON OF SLR, DEEP-SLR AND UNET
RECONSTRUCTIONS IN THE CONTEXT OF SINGLE CHANNEL RECOVERY.

(www.mridata.org) for the single channel experiments. The HCP consists of T2 weighted brain images acquired by a Siemens 3T MR scanner using a 3D Cartesian spin-echo sequence. The TE and TR parameters were 3200 ms and 565 ms respectively, while the matrix size was 320 x 256 with an FOV of 224 x 224 mm². To test the utility of the under-sampling scheme, we considered the recovery from a subset of phase encodes. Since the frequency encoding dimension is fully sampled, we perform an IFFT along this dimension and consider the recovery of each 2D slice independently. We chose thirty subjects for training, two for validation and three for testing. The knee data of twenty subjects was acquired with a 3D fast spin echo (FSE) sequence on a 3T scanner. The parameters set for the scan were: repetition time TR = 1550 ms, echo time TE=25 ms and a flip angle of 90°. There are 256 sagittal slices and 320 coronal slices per subject with a matrix size of 320 x 320 and 320 x 256 respectively at a slice thickness of 0.5mm. We chose fifteen subjects for training, two for validation and the remaining three for testing.

Parallel MRI experiments were done on multi-channel brain and knee datasets. The knee dataset [13] consists of 15-channel slices from 20 subjects with roughly 40 slices per subject. The slices are of dimension 640 x 368 x 15. A total of ten subjects were used for training, one for validation, and two for testing. The data was undersampled by varying density along the phase encodes. Brain MRI was collected from 9 subjects at the University of Iowa Hospitals using 3D T2 CUBE sequence with Cartesian readouts using a 12-channel head coil. There are 208 slices per subject with dimensions 256 x 232. We used six subjects for training, one for validation and remaining two for testing.

In both cases, the fully-sampled complex k-space data was undersampled and used for training. The complex image obtained by evaluating the inverse Fourier transforms of the individual coil data was used as ground truth in training and testing.

B. Quality Evaluation metric

We quantitatively evaluate the recovered images in terms of Signal-to-Noise ratio (SNR) and SSIM (Structural Similarity Index). The SSIM is defined in [26]. The SNR of an image is computed as $SNR = 20 \cdot \log_{10} \left(\frac{\|\mathbf{x}_{rec}\|_2}{\|\mathbf{x}_{org} - \mathbf{x}_{rec}\|_2} \right)$, where \mathbf{x}_{org} and \mathbf{x}_{rec} are original ground truth and reconstructed images respectively.

C. Architecture of the CNNs in the proposed scheme

The modular nature of the proposed scheme allows us to use any residual CNN architecture to define the prior.

1) *Single channel case*: In this work, we use a residual single input single output UNET as \mathcal{N}_k in the single channel setting for the k-space Deep-SLR scheme. We use its modified version with only twelve layers (two pooling and unpooling operations) compared to twenty in [27]. The UNET has two input and two output channels respectively, corresponding to real and imaginary parts of the Fourier data. We used the 12-layer UNET as the k-space and image-domain networks in the hybrid Deep-SLR setting. The number of parameters in both the UNETs were halved to keep the total similar to the k-space Deep-SLR network for fair comparisons.

2) *Multi-channel case*: We use a residual 5-layer MIMO CNN \mathcal{N}_k shown in Fig. 2.(b) as the k-space network. The network has thirty input and output channels, corresponding to the real and imaginary components of the fifteen coils. Each convolution layer consists of 64 3 x 3 filters, followed by ReLU non-linearity. The proposed hybrid network consists of an additional spatial domain 5-layer CNN \mathcal{N}_I . The \mathcal{N}_I block performs an IFFT (inverse Fourier transform) to feed spatial domain input ρ to the CNN and transforms the residual output back to k-space by an FFT (Fourier transform) operation. Both \mathcal{N}_k and \mathcal{N}_I are identically structured with equal number of parameters. To ensure same number of trainable parameters for comparisons, the number of filters were reduced to 32 per layer for both CNNs in hybrid Deep-SLR compared to 64 in our proposed k-space network.

We train the unrolled recursive network for different iterations K . We found $K = 10$ to be the best performing model on test data and the performance saturated afterwards. We were constrained by 16 GB GPU memory, which restricted us from going beyond 15 iterations. During training, the weights are Xavier initialized, followed by training using 500 epochs with Adam optimizer to reduce an ℓ_2 loss at a learning rate of 10^{-4} .

D. State-of-the-art methods for comparison

We compare our scheme for single-channel recovery against the SLR algorithm, a k-space UNET (K-UNET) [19], and an image domain UNET (I-UNET). The K-UNET is a direct deep learning approach with a 20-layer 2D UNET in k-space without any data-consistency steps. It accepts a real image formed by concatenation of real and imaginary parts of 2D complex k-space. The I-UNET is the spatial version of K-UNET where learning is performed in spatial domain. I-UNET structure and its number of parameters are exactly same as in K-UNET. These networks were trained and tested on single-channel knee and brain datasets described in Section IV-A.

In the parallel MRI setting, we compare the proposed scheme with MoDL [14], K-UNET [19], and the calibration-less parallel SLR algorithm, which motivated our proposed scheme. K-UNET is also a multi-channel calibrationless direct deep learning approach in k-space without any DC step [19]. Its structure is similar to single-channel K-UNET with the only difference being the multi-channel input and output. MoDL [14] is a pre-calibrated approach that uses coil sensitivity

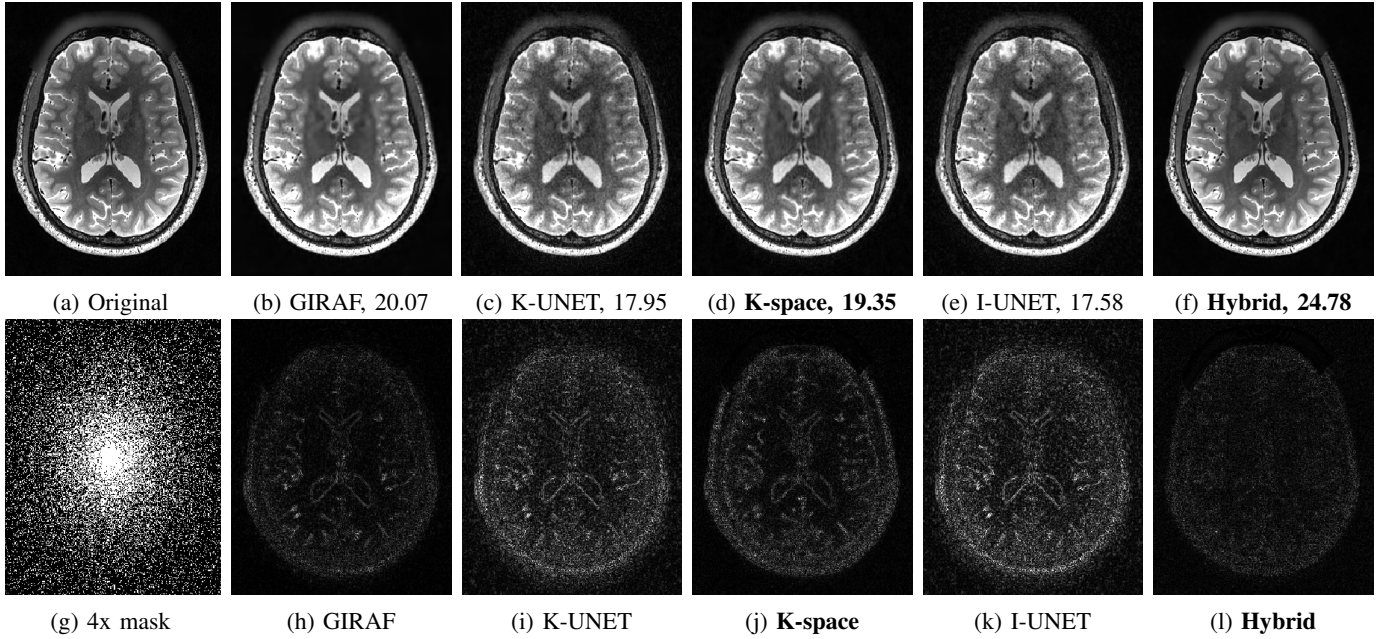


Fig. 4. Reconstruction results of 4x accelerated single-channel brain data. A Cartesian 2D non-uniform variable density undersampling was assumed. The top row (figures (a)-(f)) shows reconstructions (SOS) with SNR reported in dB while the bottom row (figures (g)-(l)) shows corresponding error images. The additional image domain prior in **Hybrid** Deep-SLR ensures significant improvement in performance over other schemes with lower magnitude of errors.

information and spatial domain regularization. All the parallel MRI methods were evaluated on both brain and knee datasets mentioned in Section IV-A.

V. RESULTS AND DISCUSSION

A. Single channel signal recovery

The comparisons of the proposed single channel scheme against state of the art methods are shown in Fig. 4 and Table I, respectively. All the methods were tested on 420 sagittal and coronal knee images from three subjects. The same set of methods were also tested on 450 brain images (three subjects). The datasets used are the ones described in Section IV-A. We observe that the k-space Deep-SLR approach in Fig. 4.(d) provides results that are roughly comparable to the model-based GIRAF method Fig. 4.(b). By contrast, the direct inversion based I-UNET and K-UNET provides lower performance, even though the number of trainable parameters are larger. Of these, the K-UNET provides slightly lower errors. The improved performance of the k-space approach over K-UNET may be attributed to the model based approach, which repeatedly enforces data-consistency. Fig. 4.(f) correspond to the hybrid deep SLR method, which uses both k-space and image domain priors. We observe that this scheme significantly reduces the errors. We note that the number of parameters in this model is similar to the one in Fig. 4.(d) since the number of output channels of each layer is halved. However, the addition of the complementary prior significantly reduces the errors.

We study the ability of the proposed k-space network to suppress artifacts, in comparison to the SLR scheme in Fig. 5. We hypothesized that the residual network learned from exemplar data will behave as a linear projector for each dataset.

We test this hypothesis in a simple setting. We note from [4], [20] that the SLR penalty in (11) is a weighted ℓ_2 norm of the gradients of the image, where the weights correspond to the sum of squares (SOS) of the estimated null-space filters. We consider a piecewise constant image in Fig. 5, which was derived from an image from the Human Connectome Project (HCP) [28], by thresholding. We note that the SOS function has low intensities in the high gradient regions of the image, while its intensity is high in the constant regions. The use of the weighted prior enables the iterative SLR algorithm to

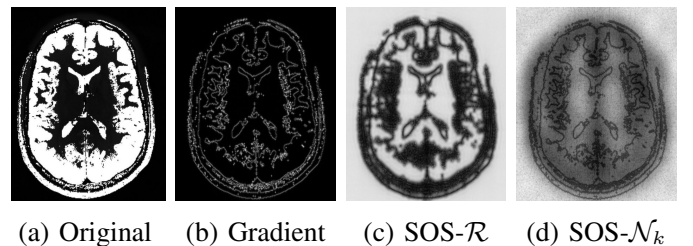


Fig. 5. Illustration of the non-linear and linear annihilation operators. The input signal are piecewise constant signals obtained by thresholding brain images. One of the images and their gradients are shown in (a) and (b), respectively. As described in the text, the application of \mathcal{R} can be viewed as weighting the gradients by the sum of squares (SoS) of the null-space filters (columns of \mathbf{Q}). The SoS function is shown in (c). Note that the SoS function is zero at the location of the edges, and hence multiplying with it will kill the image gradients. By contrast, the noise terms at spatial locations that are far away from the edges are preserved; $\mathcal{I}-\mathcal{R}$ behaves as a denoiser that preserves the signal and kills the noise and alias terms. We hypothesize that \mathcal{N}_k behaves like a linear projector to the null-space for each image. To test this hypothesis, we added pseudo-random perturbations of small magnitude to the gradients of the image and feed it to \mathcal{N}_k . The SoS of the output perturbations are shown in (d). Note that the SoS function closely mimics the linear operator \mathcal{R} in (c). Specifically, it annihilates or kills the gradient components close to the edge locations, while it preserves the noise components far away from the edges.

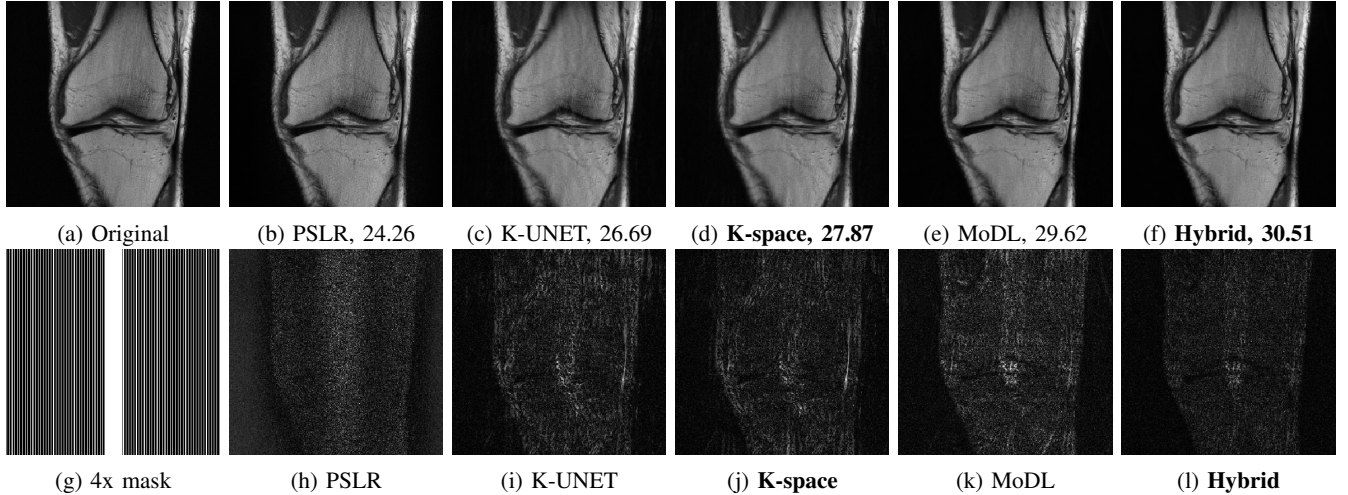


Fig. 6. Reconstruction results of 4x accelerated 15-channel knee data. A 2D cartesian structured undersampling along phase encodes was done. The top row ((a)-(f)) displays reconstructions (SOS) and the bottom row ((g)-(l)) shows corresponding error images. The numbers are SNR reported in dB. We note that the k-space based Deep-SLR scheme yields results that are comparable to the PSLR scheme. The addition of image domain prior further improves performance.

heavily penalize the gradients of the image in the constant regions, while it allows the image to have sharp edges. To compare this self-learned prior with the deep-SLR scheme, we trained a CNN network with the same architecture as above (12-layer UNET as \mathcal{N}_k) using piecewise constant brain images from 10 subjects, obtained by thresholding the HCP data. The network was then applied to the image from another subject in Fig. 5.(a), which was not included in the training process. Note that the network is non-linear. To estimate its performance as a linear operator around the image, we relied on a Monte-Carlo like approach. Specifically, we added small pseudo-random perturbations of the input image in the image domain and measured the corresponding output perturbations. We evaluated the sum of squares of the Fourier transform of the outputs for 1000 realizations, which are shown in Fig. 5.(d). Note that the sum of square output function closely mimic the SOS function in Fig. 5.(c). This experiment confirms our hypothesis that the proposed network behaves as a linear projector for each image, thus facilitating their recovery from undersampled measurements. While we observe similar results for natural images, it is difficult to visualize this due to the large dynamic range.

B. Parallel MRI image recovery

We compare the proposed schemes against state of the art calibration-less and calibrated schemes in Figures 6 and 8, and Table. II. The methods have been tested on 90 three-dimensional brain slices collected from a subject. The same set of methods have also been tested on a 100 (three subjects) 3D knee slices. Similar to the single channel setting, we observe that the performance of the Deep-SLR k-space network is comparable to the PSLR scheme. We observe that the k-space networks exhibit some residual aliasing in the knee example in Figure 6, which can be attributed to the highly structured/uniform nature of sampling. Note that the data was acquired with a calibration region, which the iterative PSLR scheme seem to have benefited from, even-though we did not explicitly rely on a calibrated approach. The table reveals that the proposed hybrid network has outperformed the multi-channel PSLR and UNET [19] and it is slightly better than pre-calibrated approach MoDL [14]. Note that MoDL is a calibrated scheme, which requires the explicit knowledge of the coil sensitivities. The coil-sensitivities are estimated from the fully-sampled region in the knee experiment in Fig. 6, while it was estimated from the fully-sampled data in the brain experiment in Fig. 8. These calibrationless methods (PSLR, Proposed and UNET) need to jointly estimate coil sensitivities and interpolate k-space. The addition of the image domain prior (hybrid Deep-SLR scheme in (f)) is seen to suppress the artifacts and provide reconstructions that are comparable to the MoDL scheme. The proposed Deep-SLR scheme facilitates the recovery of the images without the knowledge of the coil sensitivities. This approach thus eliminates the potential mismatch between the calibration scans for the estimation of the coil sensitivities and the main scan in approaches that rely on an extra calibration scans. By removing the need for an explicit calibration region, this approach enables higher acceleration factors.

The intermediate results of the hybrid Deep-SLR algorithm as a function of iterations are shown in Fig. 7. We note that the reconstructions after one and five iterations exhibit significant

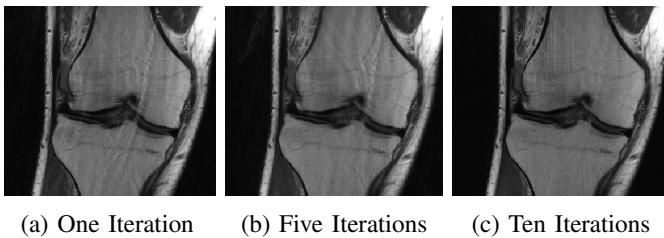


Fig. 7. Comparison of reconstruction quality of 4x undersampled multi-channel knee data for different number of iterations (K) of \mathcal{D}_k , \mathcal{D}_I and DC step. Note that the Deep-SLR parallel MRI scheme reconstructs the individual channels. The above images are the sum-of-squares reconstructions at different iterations. The aliasing artefacts decrease with increase in iterations.

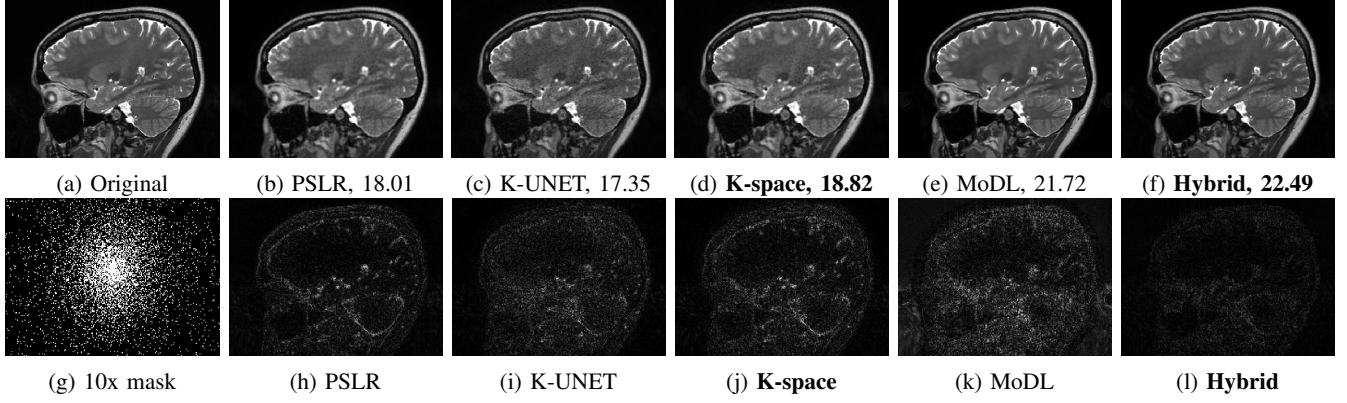


Fig. 8. Reconstruction results of 10x accelerated 12-channel brain data. The undersampling pattern was chosen to be a 2D cartesian non-uniform variable density. The numbers are SNR reported in dB. The top row ((a)-(f)) are reconstructions (SOS) while the bottom row shows error images. The **K-space** Deep-SLR has errors of lower magnitude compared to calibrationless k-space methods PSLR and K-UNET. The **Hybrid** Deep-SLR performs comparable to calibrated MoDL and shows least amount of errors among all.

aliasing, while the aliases are significantly reduced in the ten iteration model.

In Fig. 9 we compare our calibrationless hybrid Deep-SLR algorithm against the calibrated MoDL approach to demonstrate the improvement in image quality. The top two rows correspond to brain images with six fold random undersampling. The comparisons show a slight reduction in blurring, which can also be visualized in the cerebellar regions as well as the error images. Similar results are observed in the 4-fold accelerated knee images, with reduced error in the error images. The ability of the uncalibrated Deep-SLR scheme to offer similar or slightly improved image quality over the calibrated MoDL scheme can reduce potential mismatches between calibration and main scans.

C. Comparison of reconstruction times

Another key benefit of the proposed Deep-SLR scheme over SLR methods is the quite significant reduction in run-time, on top of the improved performance offered by the combination of the image domain prior. The recorded run times are shown in Table III. We report run times for 10 iterations ($K=10$) of our proposed k-space, hybrid Deep-SLR algorithms and MoDL. We note that the deep learning approaches are roughly few thousands fold faster than the IRLS SLR schemes in both cases. As discussed previously, SLR methods estimate the linear projection operator on the fly. At each iteration, the SLR schemes estimate the null-space using (10), which involves the evaluation of the Gram matrix $\mathcal{T}(\mathcal{G}(\hat{\rho}^{(n)}))^H \mathcal{T}(\mathcal{G}(\hat{\rho}^{(n)}))$

Acceleration	Brain				Knee	
	6x		10x		4x	
Methods	SNR	SSIM	SNR	SSIM	SNR	SSIM
PSLR	21.02	0.942	18.12	0.918	24.26	0.873
K-UNET	19.58	0.920	17.28	0.883	26.81	0.887
K-space	21.58	0.951	18.71	0.921	27.87	0.904
MoDL	23.30	0.938	21.63	0.913	29.77	0.928
Hybrid	24.34	0.958	22.20	0.935	30.57	0.944

TABLE II
QUANTITATIVE COMPARISON OF PSLR, MODL, PROPOSED AND UNET RECONSTRUCTIONS IN TERMS OF SNR (dB) AND SSIM.

and its singular value decomposition (SVD). In addition, the SLR schemes require atleast 50 iterations to converge. The high complexity of the SVD and the evaluation of the Gram matrix, along with the large number of iterations, is the main reason for the long run-time of the SLR methods. By contrast, the Deep-SLR approaches pre-learn the CNNs from exemplar data, which eliminates the need for (10). The hybrid Deep-SLR approach is slightly slower than k-space Deep-SLR in both the cases since the former uses two CNNs compared to the one by

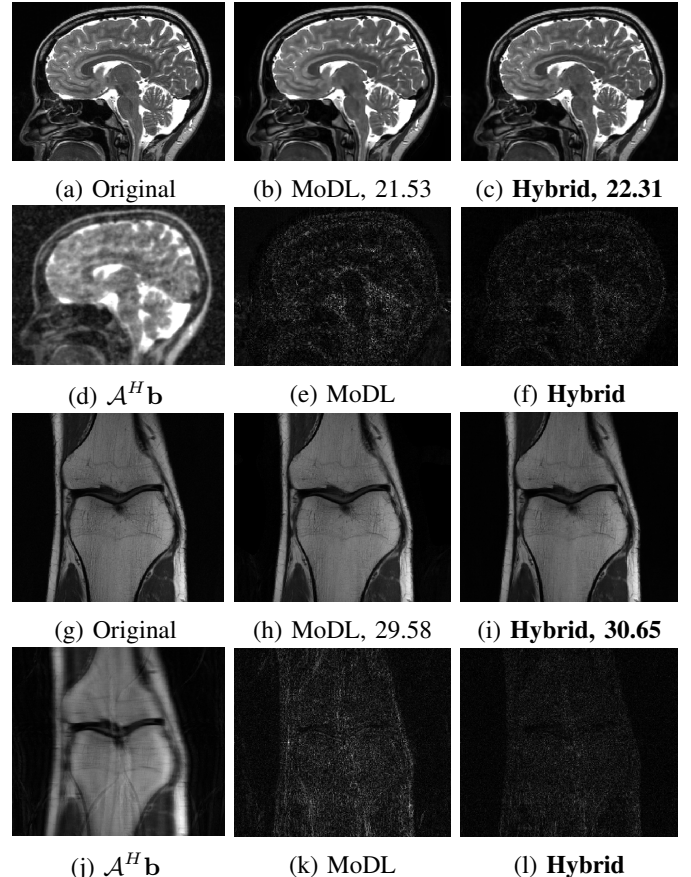


Fig. 9. Proposed calibrationless **Hybrid** Deep-SLR vs calibrated scheme MoDL. The figures (a)-(f) and (g)-(l) correspond to 6x undersampled 12-channel Brain and 4x undersampled 15-channel Knee reconstructions (SOS) respectively. The numbers are SNR in dB. The **Hybrid** Deep-SLR shows lesser errors with lower magnitude compared to MoDL.

Single-channel recovery					
Organ	GIRAF	K-UNET	K-space	I-UNET	Hybrid
Knee/Brain	37s	0.013s	0.06s	0.013s	0.07s
Parallel MRI recovery					
Organ	PSLR	K-UNET	K-space	MoDL	Hybrid
Brain	367s	0.21s	0.05s	0.25s	0.058s
Knee	932s	0.85s	0.19s	1.32s	0.27s

TABLE III

COMPARISON OF SINGLE-CHANNEL AND PARALLEL MRI RECONSTRUCTION TIMES. THE RECORDED RUN TIMES ARE IN SECONDS.

latter even if the effective number of parameters are same. In single-channel setting, although K-UNET and I-UNET have more learnable parameters, these approaches are faster by virtue of single iteration compared to multiple iterations in proposed schemes. Note that the iterative approach brings in improved performance as discussed in the previous sections. In the parallel MRI setting, the Deep-SLR schemes use 5-layer CNNs that make them faster than K-UNET even after multiple iterations. We note that the MoDL scheme uses a multi-channel forward model requires conjugate gradients (CG) algorithms to enforce data-consistency, which makes it slower than the Deep-SLR schemes. By contrast, the proposed scheme recovers the coil images; the forward model only includes Fourier sampling, which makes these schemes faster in training and testing.

VI. CONCLUSION

We introduced a general model based deep learning framework for structured low rank matrix completion algorithms. We show that an IRLS solution to SLR methods have a recursive network structure, which alternates between data-consistency enforcement and the projection to the signal subspace, performed by a linear convolutional filterbank. We rely on CNN to perform the projection, whose parameters are learned from exemplar data in an end-to-end fashion. The proposed scheme reduces the computational complexity of SLR algorithms by several orders of magnitude. In addition, an additional image domain prior helps to further improve performance. We show the utility of the proposed scheme in two representative applications with drastically different lifting structure. Hence, the proposed framework is generally applicable to a wide range of SLR priors.

REFERENCES

- [1] M. Lustig, D. Donoho, and J. M. Pauly, "Sparse mri: The application of compressed sensing for rapid mr imaging," *Magnetic Resonance in Medicine: An Official Journal of the International Society for Magnetic Resonance in Medicine*, vol. 58, no. 6, pp. 1182–1195, 2007.
- [2] M. Jacob, M. P. Mani, and J. C. Ye, "Structured low-rank algorithms: Theory, mr applications, and links to machine learning," *arXiv preprint arXiv:1910.12162*, 2019.
- [3] J. P. Haldar and K. Setsompop, "Linear predictability in mri reconstruction: Leveraging shift-invariant fourier structure for faster and better imaging," *arXiv preprint arXiv:1903.03141*, 2019.
- [4] G. Ongie and M. Jacob, "Super-resolution mri using finite rate of innovation curves," in *IEEE Int. Symp. Bio. Imag.* IEEE, 2015, pp. 1248–1251.
- [5] D. Lee, K. H. Jin, E. Y. Kim, S.-H. Park, and J. C. Ye, "Acceleration of mr parameter mapping using annihilating filter-based low rank hankel matrix (aloha)," *Magnetic resonance in medicine*, vol. 76, no. 6, pp. 1848–1864, 2016.
- [6] Uecker *et al.*, "ESPIRiT - An eigenvalue approach to autocalibrating parallel MRI: Where SENSE meets GRAPPA," *Magnetic Resonance in Medicine*, vol. 71, no. 3, pp. 990–1001, 2014.
- [7] M. Mani, M. Jacob, D. Kelley, and V. Magnotta, "Multi-shot sensitivity-encoded diffusion data recovery using structured low-rank matrix completion (mussels)," *Magnetic resonance in medicine*, vol. 78, no. 2, pp. 494–507, 2017.
- [8] G. Ongie and M. Jacob, "A fast algorithm for convolutional structured low-rank matrix recovery," *IEEE transactions on computational imaging*, vol. 3, no. 4, pp. 535–550, 2017.
- [9] J. C. Ye, Y. Han, and E. Cha, "Deep convolutional framelets: A general deep learning framework for inverse problems," *SIAM Journal on Imaging Sciences*, vol. 11, no. 2, pp. 991–1048, 2018.
- [10] K. H. Jin, M. T. McCann, E. Froustey, and M. Unser, "Deep convolutional neural network for inverse problems in imaging," *IEEE Transactions on Image Processing*, vol. 26, no. 9, pp. 4509–4522, 2017.
- [11] M. Akçakaya, S. Moeller, S. Weingärtner, and K. Uğurbil, "Scan-specific robust artificial-neural-networks for k-space interpolation (raki) reconstruction: Database-free deep learning for fast imaging," *Magnetic resonance in medicine*, vol. 81, no. 1, pp. 439–453, 2019.
- [12] J. Sun, H. Li, Z. Xu *et al.*, "Deep admn-net for compressive sensing mri," in *Advances in neural information processing systems*, 2016, pp. 10–18.
- [13] Hammernik *et al.*, "Learning a variational network for reconstruction of accelerated mri data," *Magnetic resonance in medicine*, vol. 79, no. 6, pp. 3055–3071, 2018.
- [14] H. K. Aggarwal, M. P. Mani, and M. Jacob, "Modl: Model-based deep learning architecture for inverse problems," *IEEE transactions on medical imaging*, vol. 38, no. 2, pp. 394–405, 2018.
- [15] T. Eo, Y. Jun, T. Kim, J. Jang, H.-J. Lee, and D. Hwang, "Kiki-net: cross-domain convolutional neural networks for reconstructing undersampled magnetic resonance images," *Magnetic resonance in medicine*, vol. 80, no. 5, pp. 2188–2201, 2018.
- [16] Shin *et al.*, "Calibrationless parallel imaging reconstruction based on structured low-rank matrix completion," *Magnetic resonance in medicine*, vol. 72, no. 4, pp. 959–970, 2014.
- [17] H. K. Aggarwal, M. P. Mani, and M. Jacob, "Modl-mussels: Model-based deep learning for multishot sensitivity-encoded diffusion mri," *IEEE transactions on medical imaging*, 2019.
- [18] A. Pramanik, H. Aggarwal, and M. Jacob, "Off-the-grid model based deep learning (o-modl)," in *2019 IEEE 16th International Symposium on Biomedical Imaging (ISBI 2019)*. IEEE, 2019, pp. 1395–1398.
- [19] Y. Han and J. C. Ye, "k-space deep learning for accelerated mri," *arXiv preprint arXiv:1805.03779*, 2018.
- [20] G. Ongie, S. Biswas, and M. Jacob, "Convex recovery of continuous domain piecewise constant images from nonuniform fourier samples," *IEEE Transactions on Signal Processing*, vol. 66, no. 1, pp. 236–250, 2017.
- [21] Griswold *et al.*, "Generalized autocalibrating partially parallel acquisitions (grappa)," *Magnetic Resonance in Medicine: An Official Journal of the International Society for Magnetic Resonance in Medicine*, vol. 47, no. 6, pp. 1202–1210, 2002.
- [22] M. Lustig and J. M. Pauly, "Spirit: iterative self-consistent parallel imaging reconstruction from arbitrary k-space," *Magnetic resonance in medicine*, vol. 64, no. 2, pp. 457–471, 2010.
- [23] G. Ongie and M. Jacob, "Off-the-Grid Recovery of Piecewise Constant Images from Few Fourier Samples," *SIAM on Imag. Sci.*, vol. 9, no. 3, pp. 1004–1041, 2016.
- [24] D. Lee, J. Yoo, S. Tak, and J. C. Ye, "Deep residual learning for accelerated mri using magnitude and phase networks," *IEEE Transactions on Biomedical Engineering*, vol. 65, no. 9, pp. 1985–1995, 2018.
- [25] J. Schlemper, J. Caballero, J. V. Hajnal, A. N. Price, and D. Rueckert, "A deep cascade of convolutional neural networks for dynamic mr image reconstruction," *IEEE transactions on Medical Imaging*, vol. 37, no. 2, pp. 491–503, 2017.
- [26] Z. Wang, A. C. Bovik, H. R. Sheikh, E. P. Simoncelli *et al.*, "Image quality assessment: from error visibility to structural similarity," *IEEE transactions on image processing*, vol. 13, no. 4, pp. 600–612, 2004.
- [27] O. Ronneberger, P. Fischer, and T. Brox, "U-net: Convolutional networks for biomedical image segmentation," in *International Conference on Medical Image Computing and Computer-Assisted Intervention (MICCAI)*. Springer, 2015, pp. 234–241.
- [28] Essen *et al.*, "The human connectome project: a data acquisition perspective," *Neuroimage*, vol. 62, no. 4, pp. 2222–2231, 2012.